

**Superconductivity enhanced in the polar metal region of
 $\text{Sr}_{0.95}\text{Ba}_{0.05}\text{TiO}_3$ and $\text{Sr}_{0.985}\text{Ca}_{0.015}\text{TiO}_3$
revealed by the systematic Nb doping.**

Yasuhide Tomioka, Naoki Shirakawa, and Isao H. Inoue¹

National Institute of Advanced Industrial Science and Technology (AIST),
Tsukuba 305-8565, Japan

Different ferroelectrics, $\text{Sr}_{0.95}\text{Ba}_{0.05}\text{TiO}_3$ and $\text{Sr}_{0.985}\text{Ca}_{0.015}\text{TiO}_3$, turn into metallic with centrosymmetry breaking by the electron doping. The systematic substitution of Nb^{5+} for Ti^{4+} has revealed that the two polar metals commonly exhibit a simple superconducting dome with a single convex. Interestingly, the superconducting transition temperature T_c is more enhanced in these polar metals compared with the non-polar matrix $\text{Sr}(\text{Ti},\text{Nb})\text{O}_3$. The maximum T_c reaches 0.75 K, the highest in the families of SrTiO_3 ever reported. However, the T_c enhancement is unexpectedly lower in the vicinity of the ferroelectric quantum critical point (QCP). It becomes much more prominent by further going into the dilute carrier-density region, where the screening is less effective. The results suggest that the centrosymmetry breaking, i.e., the ferroelectric nature, does not kill the superconductivity. It rather directly enhances the superconductivity without the help of quantum fluctuation.

¹email: isaocaius@gmail.com

Are superconductivity and ferroelectricity reconcilable? Matthias, a pioneer in the search for superconducting materials, put it a half-century ago¹ that “superconductivity and ferroelectricity will exclude one another.” This speculation is called the Matthias Conjecture, an old guideline for hunting new superconducting materials. Interestingly, the strife of superconductivity and ferroelectricity motivated the study of Bednorz and Müller to discover the high-temperature cuprate superconductor². Anderson and Blount suggested that some metals can be ferroelectric in the sense of broken inversion symmetry. However, almost all the ferroelectrics are highly insulating, and only a few materials have been experimentally alleged as the Anderson-Blount-type ferroelectric (polar) metals³. Those so-called polar metals have recently stirred the research community^{4–21}. Especially, low-carrier-density polar metals have gained attraction^{22,23} because they show superconductivity against Matthias Conjecture. Our study focuses on one of them, perovskite-type titanate SrTiO₃, to reveal a new aspect of superconductivity with ferroelectricity.

The single crystal of SrTiO₃ shows a huge relative permittivity of about 42000 at 4.2 K (ref.²⁴). However, the ferroelectric phase transition does not happen above 35 mK (ref.²⁵). Since the ground state is predicted to be ferroelectric^{26,27}, it is believed that the strong quantum fluctuation suppresses the ferroelectricity²⁵. However, the picture does not explain the unusual minimum in the inverse relative permittivity of SrTiO₃ (refs.^{28,29}), and the origin of the paraelectric state is still in the intensive debate. In any case, the paraelectric state is quite fragile; a small amount of homovalent substitution of Ca²⁺ (refs.^{30,31}) or Ba²⁺ (refs.^{32,33}) for Sr²⁺ turns SrTiO₃ into ferroelectric. The ¹⁸O isotope exchange for ¹⁶O also results in the ferroelectric phase (refs.^{10,34}). Domain walls of SrTiO₃ in the tetragonal phase carry polar properties related to the ferroelectricity^{35,36}. Furthermore, epitaxial strain^{18,19,37,38} and Sr defect³⁹ for the thin film of SrTiO₃ generate ferroelectricity.

On the other hand, the electron doping of SrTiO₃, e.g., substitution of La³⁺ or Sm³⁺ for Sr²⁺ (refs.^{4–7,40,41}), Nb⁵⁺ for Ti⁴⁺ (refs.^{21,42–44}), or removal of O²⁻ (refs.^{9–12,45–50}), makes SrTiO₃ metallic. In all these cases, superconductivity appears at low temperatures. (As for Nb doping, we write it as Nb:SrTiO₃ in this paper, if it is not necessary to express explicitly as SrTi_{1-x}Nb_xO₃.) A recent tunnelling study revealed that Ti 3d t_{2g} orbitals generate two light bands and one heavy band⁴⁴. The electrons in the heavy band have the largest contribution to the superconductivity⁴⁴. The most interesting property of the doped SrTiO₃ systems is that they are extremely low carrier-density superconductors with the Fermi energy a few orders of magnitude smaller than the phonon energy. Because the Migdal-Eliashberg criterion (adiabatic condition) is violated^{22,23}, superconducting pairing interaction should have a significant frequency dependence due to the poor screening of the Coulomb repulsion²³. Further doping makes the Fermi energy larger, but

the superconductivity disappears above the carrier density of 10^{21} cm^{-3} , resulting in the dome-like dependence of the superconducting transition temperature against the carrier density^{4,45–47}.

The physical mechanism behind these phenomena has challenged the microscopic theory for more than half a century. Although there has been no compelling picture encompassing the disparate ideas, some unconventional mechanisms have recently sparked research in this field. Typical examples are the Cooper pairing driven by longitudinal optical (LO) phonons⁵¹, by a soft transverse optical (TO) mode via two phonons⁵², which also explains the T^2 -dependence of resistivity very well^{53,54}, by plasmon and plasmon-polariton coupling^{55,56}, and by the ferroelectric fluctuations^{15,16,23,27}, including the odd-frequency pair correlations due to the intrinsic spin-orbit coupling and polar inversion symmetry breaking¹⁷. There were also remarkable experimental discoveries; carrier doping of two ferroelectric matrices, $(\text{Sr,Ca})\text{TiO}_3$ (refs.^{10–12}) and $\text{SrTi}({}^{16}\text{O}, {}^{18}\text{O})_3$ (refs.^{4,9,10}), raises the transition temperature T_c higher than that of SrTiO_3 matrix, suggesting that the superconductivity seems to be enhanced in the ferroelectric SrTiO_3 . Several experimental investigations for SrTiO_3 with epitaxial strain are noteworthy^{5–7,41}; the strain breaks the spatial inversion symmetry and enhances the spin-orbit interactions^{5,6}. Then, T_c goes up to 0.6 K (ref.⁵). Surprisingly, although T_c is very small in the SrTiO_3 systems, magnetic impurities, e.g., Sm and Eu, have no effects on T_c (ref.⁴¹).

We have studied two different polar metals: $\text{Sr}_{0.95}\text{Ba}_{0.05}\text{TiO}_3$ and $\text{Sr}_{0.985}\text{Ca}_{0.015}\text{TiO}_3$ with Nb^{5+} for Ti^{4+} for the carrier density of $\sim 10^{18}$ to $\sim 10^{21} \text{ cm}^{-3}$. $\text{Sr}_{0.95}\text{Ba}_{0.05}\text{TiO}_3$ exhibits Ti-site dominated ferroelectricity in which Ti-O hybridisation gives rise to a strong pseudo- or second-order Jahn-Teller distortion¹³. The Curie temperature is ~ 50 K with the polarisation direction along [111] of a pseudo-cubic lattice. On the other hand, $\text{Sr}_{0.985}\text{Ca}_{0.015}\text{TiO}_3$ shows Sr-site dominated ferroelectricity originated from the off-centre position of Ca^{2+} with a smaller ionic radius than that of Sr^{2+} (refs.^{11–14}). The Curie temperature is ~ 30 K with the polarisation direction [110] (ref.³⁰). We demonstrate that the two polar metals show a simple superconducting dome with a larger T_c . We also reveal that the T_c increase rate around the ferroelectric quantum critical point is much lower than the rate in the polar region.

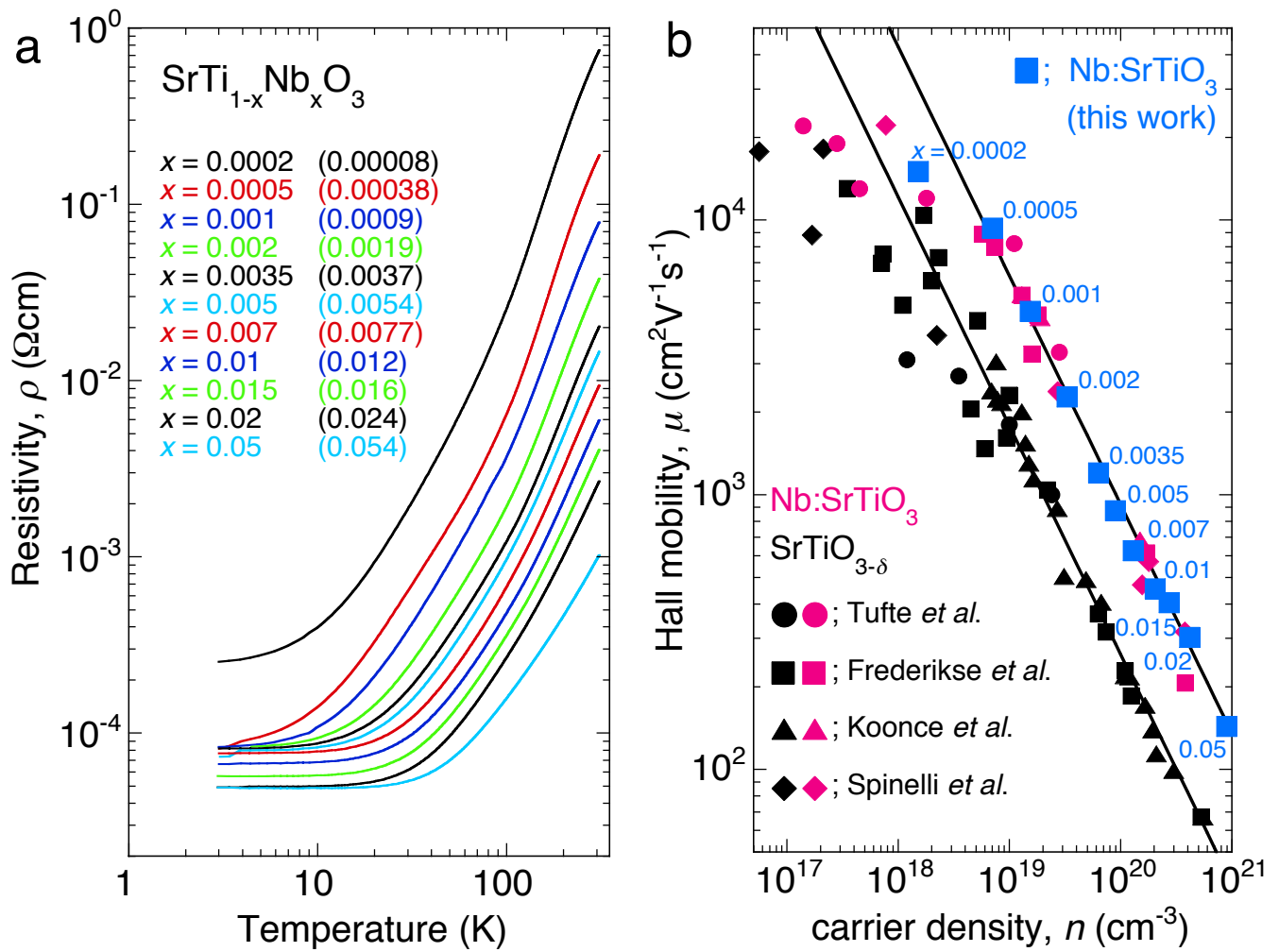


Fig. 1 | Resistivity and Hall mobility of Nb:SrTiO₃ single crystals. **a**, Temperature dependence of the resistivity with the nominal Nb content x of 0.0002, 0.0005, 0.001, 0.002, 0.005, 0.007, 0.01, 0.015, 0.02, and 0.05 from the room temperature down to 3 K. The number of Ti $3d$ electrons deduced from the Hall-effect measurements are noted in parenthesis. **b**, Hall mobility of our samples (blue symbols), that of SrTiO_{3- δ} (black symbols) and Nb:SrTiO₃ (red symbols) (refs. ^{42,57–59}). Solid lines represent a phenomenological model⁶⁰, $\mu \propto n^{-\frac{5}{6}}$, that fits the experimental data very well.

The evolution of the metallic state of our Nb:SrTiO₃ single crystals (see Methods for the details of our sample preparations) is shown in Fig. 1a. The results are similar to those reported by Tufte et al.⁵⁷, but our samples show much smaller residual resistivity. The Hall effect measurements (see Supplementary Information) have deduced the carrier density n and the Hall mobility μ at 5 K (Fig. 1b). The values of μ for SrTiO_{3- δ} and Nb:SrTiO₃ in the literature^{42,57-59} are also plotted for comparison. Behnia proposed a model⁶⁰, assuming that the mean-free path is proportional to the average distance between dopants and the Thomas-Fermi screening length, giving $\mu \propto n^{-\frac{5}{6}}$. Our data in Fig. 1b fit the model pretty well. In the model, the proportionality factor depends on the reciprocal of the effective mass and the dopant potential. Because μ of our Nb:SrTiO₃ is much larger than that of SrTiO_{3- δ} , the dopant potential is shallower for the Nb:SrTiO₃. By creating oxygen defects, one or two electrons are trapped at each oxygen-vacancy site and localised without contributing to the itinerant carriers^{60,61}. On the other hand, in the Ti/Nb substitution, the replacement of the Ti 3d orbitals by the Nb 4d ones does not change the orbital characteristics so that the disorder is smaller than the oxygen defects formation. This larger mobility is expected to raise the superconducting critical temperature because the spatial disorder generally destroys the superconducting state and suppresses T_c (ref.⁶²).

The resistive transition of the superconductivity of our Nb:SrTiO₃ single crystals (same samples in Fig. 1a) is shown in Fig. 2a. We have defined T_c as the mid-point of the resistive transition⁴, plotted as a function of the carrier density n at 5K in Fig. 2b. Supplementary Information describes that the carrier density in the non-polar metallic state depends little on temperature. The T_c values of SrTiO_{3- δ} (refs.^{12,45}), Nb:SrTiO₃ (ref.²²), and (Sr,La)Ti(¹⁶O_{1-z}¹⁸O_z)₃ (refs.^{4,40}) are also plotted for comparison. Our data have clearly demonstrated that the superconducting dome of Nb:SrTiO₃ is shifted toward a higher T_c and larger n region than the superconducting dome of (Sr,La)TiO₃. The optimal T_c of our Nb:SrTiO₃ is ~ 0.5 K at $n \simeq 1 \times 10^{20}$ cm⁻³.

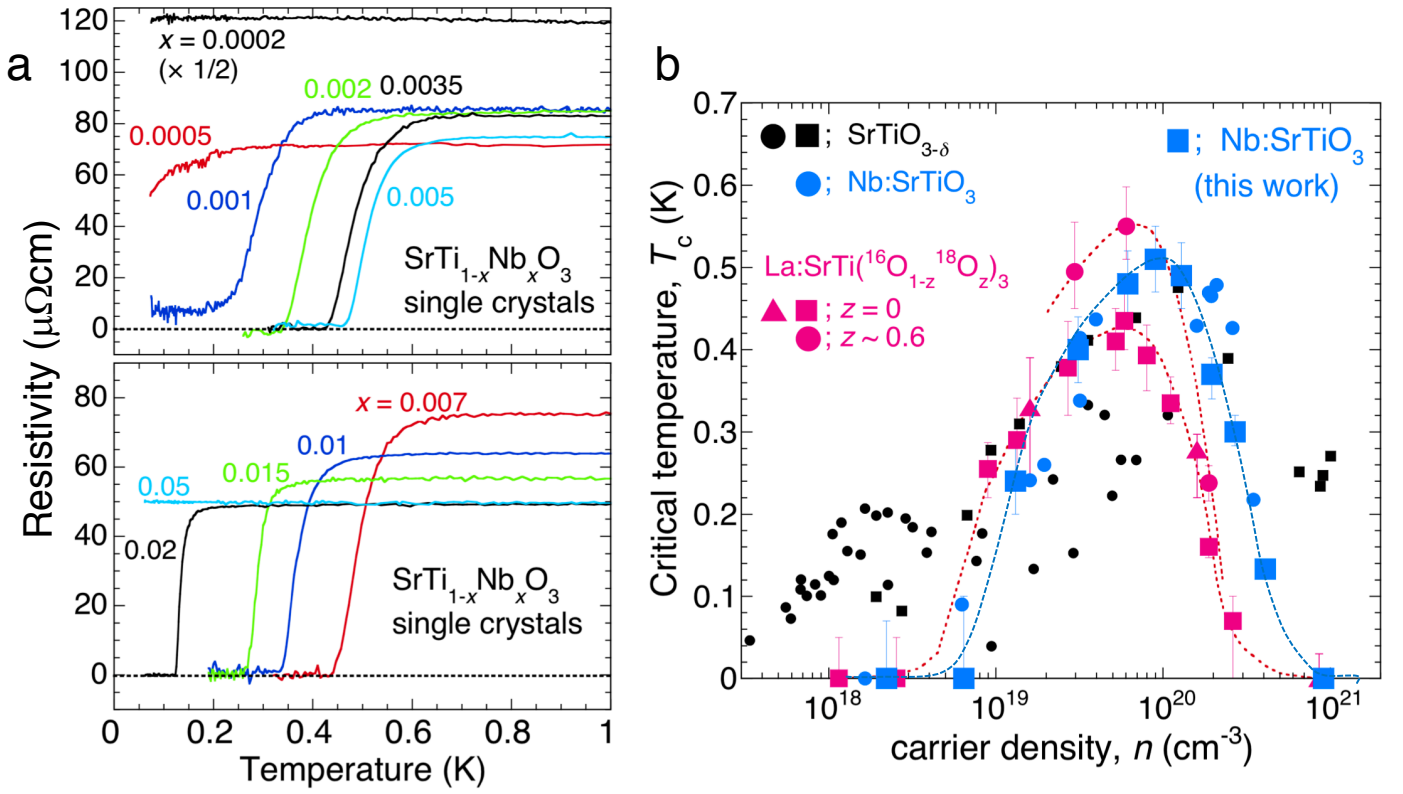


Fig. 2 | Superconducting domes of $\text{SrTiO}_{3-\delta}$, $(\text{Sr,Lu})\text{TiO}_3$, and Nb:SrTiO_3 . **a**, Resistivity of our $\text{SrTi}_{1-x}\text{Nb}_x\text{O}_3$ single crystals (same samples in Fig. 1a) below 1 K for $0.0002 \leq x \leq 0.005$ (upper panel) and $0.007 \leq x \leq 0.05$ (lower panel). The $x = 0.0005$ sample shows a symptom of superconductivity below around 0.2 K, but zero resistivity was not achieved at the lowest temperature measured. The value of T_c increases with x up to $x = 0.005$ and decreases for $x \geq 0.007$. **b**, Superconducting domes of Nb:SrTiO_3 obtained by this work (blue closed squares). Those of our other works for $(\text{Sr,Lu})\text{TiO}_3$ (red closed squares⁴) and $(\text{Sr,Lu})\text{Ti}({}^{16}\text{O}_{0.4}\text{}^{18}\text{O}_{0.6})_3$ (red closed circles⁴) are also plotted. Dashed lines are a guide for the eyes. The upper and lower error bars are the onset and end temperatures of the slope for the superconducting phase transition, same as in ref.⁴ For comparison, other data in the literature are included in the plot: Nb:SrTiO_3 (blue closed circles²²), $(\text{Sr,Lu})\text{TiO}_3$ (red closed triangles⁴⁰) and $\text{SrTiO}_{3-\delta}$ (black closed squares⁴⁵ and circles¹²).

There are two noticeable differences in the superconducting dome of some $\text{SrTiO}_{3-\delta}$ samples in the literature and the domes of our $(\text{Sr},\text{La})\text{TiO}_3$ and $\text{Nb}:\text{SrTiO}_3$ samples. The first prominent difference is a shoulder peak at $n \simeq 1.2 \times 10^{18} \text{ cm}^{-3}$ in $\text{SrTiO}_{3-\delta}$ (ref.¹²). If the three-fold degeneracy of the t_{2g} band is lifted⁴⁷ and each band has a different filling, it is likely to observe a superconducting dome for each band. However, neither in our $(\text{Sr},\text{La})\text{TiO}_3$ nor $\text{Nb}:\text{SrTiO}_3$ shows the shoulder peak, seemingly suggesting only the heavy band of Ti $3d$ have the contribution to the superconductivity⁴⁴. The second difference is seen in the large n region ($n \simeq 1 \times 10^{21} \text{ cm}^{-3}$), where superconductivity of $T_c \simeq 0.25 \text{ K}$ was reported for $\text{SrTiO}_{3-\delta}$ (ref.⁴⁵). In this case, as well, neither of our $(\text{Sr},\text{La})\text{TiO}_3$ nor $\text{Nb}:\text{SrTiO}_3$ shows superconductivity. One of the possible explanations for both differences simultaneously is to consider the inhomogeneity of the oxygen vacancies⁴⁸. The thermal reduction procedure for the $\text{SrTiO}_{3-\delta}$ single crystal to create the oxygen vacancies is restricted to dislocation⁶³ as the formation enthalpy of oxygen vacancies near the dislocations is significantly lower than that in the stoichiometric SrTiO_3 matrix⁶⁴. Thus, the inhomogeneous carrier density distribution happens in the $\text{SrTiO}_{3-\delta}$ sample. The Hall measurement gives the averaged carrier density of the bulk, whereas the observed T_c reflects the highest T_c among the percolation paths of the doped regions where the carrier density is different from the average one.

Now that we know, compared with $(\text{Sr},\text{La})\text{TiO}_3$ and $\text{SrTiO}_{3-\delta}$, our $\text{Nb}:\text{SrTiO}_3$ shows higher mobility and higher T_c with the simple single superconducting dome. These results mean Nb-doping to the ferroelectric derivatives of SrTiO_3 is a solid strategy to investigate the relationship between ferroelectricity and superconductivity. Therefore, we focus on the two ferroelectric matrices: $\text{Sr}_{0.985}\text{Ca}_{0.015}\text{TiO}_3$ and $\text{Sr}_{0.95}\text{Ba}_{0.05}\text{TiO}_3$. Interestingly, the types of ferroelectricity of the two matrices are pretty different.

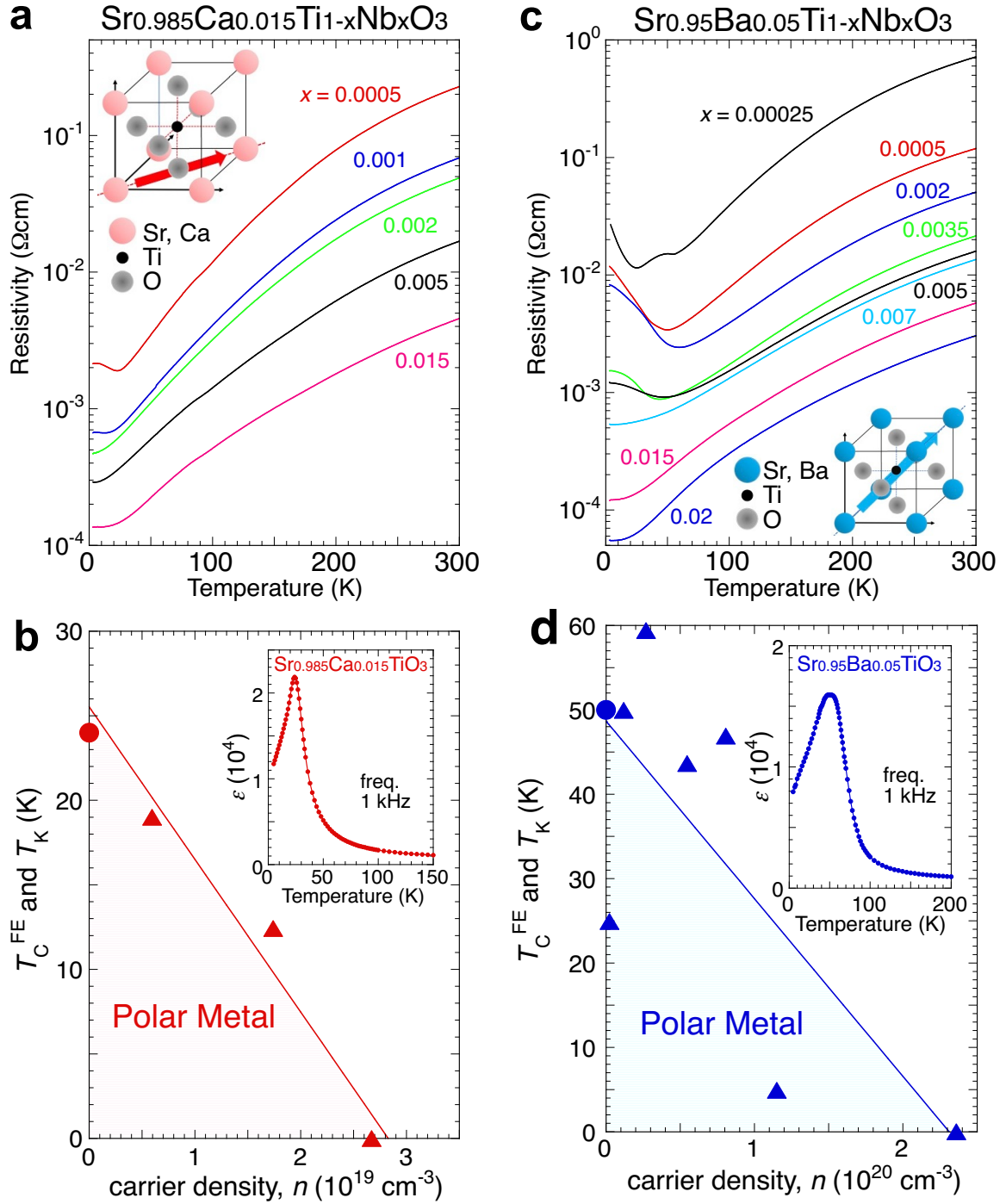


Fig. 3 | Resistance anomaly as the evidence of polar metal. **a**, Resistivity of our $\text{Sr}_{0.985}\text{Ca}_{0.015}\text{Ti}_{1-x}\text{Nb}_x\text{O}_3$ single crystals with $x = 0.0005, 0.001, 0.002, 0.005,$ and 0.015 plotted against T . **b**, Curie temperature $T_C^{\text{FE}} \sim 25$ K of the ferroelectric transition for undoped $\text{Sr}_{0.985}\text{Ca}_{0.015}\text{TiO}_3$ (red closed circle) and the temperatures T_K at which the resistivity shows anomaly for doped samples (red closed triangles) are plotted as a function of the carrier density n at room temperature. The solid line represents the least-square fit of T_K . The line is almost close to T_C^{FE} at zero carrier density. Inset shows the temperature dependence of the relative permittivity ϵ , where the peak corresponds to T_C^{FE} of ~ 25 K. The value is almost equal to that evaluated by $T_C^{\text{FE}} = A(y - 0.0018)^{1/2}$ ($A = 298$ K, and $y = 0.015$) (ref.³⁰). **c**, Resistivity of our $\text{Sr}_{0.95}\text{Ba}_{0.05}\text{Ti}_{1-x}\text{Nb}_x\text{O}_3$ single crystals with $x = 0.00025, 0.0005, 0.002, 0.0035, 0.005, 0.007, 0.015,$ and 0.02 . **d**, $T_C^{\text{FE}} \sim 50$ K for undoped $\text{Sr}_{0.95}\text{Ba}_{0.05}\text{TiO}_3$ (blue closed circle), which corresponds to the peak of ϵ (inset), and the temperatures for resistance anomaly for doped ones (blue closed triangles) are plotted against n . The solid line represents the least-square fit of T_K .

In (Sr,Ca)TiO₃, the ferroelectricity is driven by the dipole-dipole interaction between the off-centred Ca sites with smaller ionic radii than the Sr²⁺ ion¹³. Nb-doping makes it highly conductive, but the resistivity increases slowly as T decreases at low temperature (Fig. 3a). On the contrary, our non-polar Nb:SrTiO₃ single crystal does not show the resistance anomaly at all. The temperatures T_K at which the resistance anomaly occurs are plotted against n at room temperature, which fit the solid line in Fig. 3b fairly well. Intriguingly, ferroelectric Curie temperature $T_C^{\text{FE}} \sim 25$ K, corresponding to the sharp peak of the relative permittivity ϵ (inset of Fig. 3b), locates on the same line. This correspondence means that T_K is the remnant of T_C^{FE} even in the metallic region, and the Nb:Sr_{0.985}Ca_{0.015}TiO₃ is a polar metal in the hatched region. That is, the dipole moment remains at the off-centred Ca site because of the poor screening, and the glassy dipole-dipole interaction (between the Ca sites) may cause the resistance anomaly. The static interaction is fully screened ($T_K = 0$) at n^* of $\sim 2.8 \times 10^{19}$ cm⁻³. This experimental value of n^* is almost equivalent to $n^* = 3.3 \times 10^{19}$ cm⁻³ calculated by assuming a Thomas-Fermi screening length of the itinerant carriers compared with the averaged dipole-dipole distance¹⁴.

On the other hand, in (Sr,Ba)TiO₃, the Ba²⁺ ion hardly moves due to its larger ionic radius and heavier mass than the Sr²⁺ ion. Therefore, the phonon softening through the pseudo- or second-order Jahn-Teller distortion due to the sizeable Ti-O hybridisation becomes the central mechanism of the ferroelectricity¹³. This is different in principle from the mechanism of the ferroelectricity in (Sr,Ca)TiO₃. Our Sr_{0.95}Ba_{0.05}TiO₃ single crystal shows the ferroelectric transition at $T_C^{\text{FE}} \sim 50$ K (inset of Fig. 3d) accompanied by a structural change from cubic $Pm\bar{3}m$ to rhombohedral $R\bar{3}m$ (ref.³²). We did the powder x-ray diffraction for our metallic Sr_{0.95}Ba_{0.05}Ti_{0.998}Nb_{0.002}O₃ at 10 K, and the results were examined by the Rietveld analysis (see Supplementary Information). The pattern was, in fact, consistent with the rhombohedral $R\bar{3}m$ symmetry with the displacement of Ti along the [111] axis of a pseudo-cubic lattice. The spatial inversion symmetry is broken, and we call the metallic state is polar. To our surprise, although the origin of the ferroelectricity is different from the Nb:Sr_{0.985}Ca_{0.015}TiO₃, the resistance anomaly is similarly observed in the Nb:Sr_{0.95}Ba_{0.05}TiO₃ (Fig. 3c), and the value of T_K decreases with n (Fig. 3d). The carrier-density dependence does not seem as linear as seen in Nb:Sr_{0.985}Ca_{0.015}TiO₃, but assuming the linear relationship of T_K and n for simplicity, the line reaches almost to T_C^{FE} at zero carrier density. We have estimated the critical carrier density of $n^* \sim 2.3 \times 10^{20}$ cm⁻³ for $T_K = 0$. This value is one order larger than that of Nb:Sr_{0.985}Ca_{0.015}TiO₃, although the difference of T_C^{FE} is only a factor of two.

It should be noted that, below around T_K , the carrier density n for Nb:Sr_{0.95}Ba_{0.05}TiO₃ decreases with temperature (see Supplementary Information) similarly to that reported in ref.⁵. This means some carriers are bound to the local dipole moment for screening. On the other hand,

the values of n above T_K do not depend on temperature and are almost similar to n at room temperature. The critical carrier density n^* , where the resistance anomaly disappears, may represent the so-called ferroelectric quantum critical point (QCP). If so, it is pretty intriguing that our two systems, Nb:Sr_{0.985}Ca_{0.015}TiO₃ and Nb:Sr_{0.95}Ba_{0.05}TiO₃, have different ferroelectric mechanisms, and the ferroelectric QCPs are one order different. Do those differences affect the appearance of superconductivity? From here on, we investigate systematically the superconductivity of the two systems.

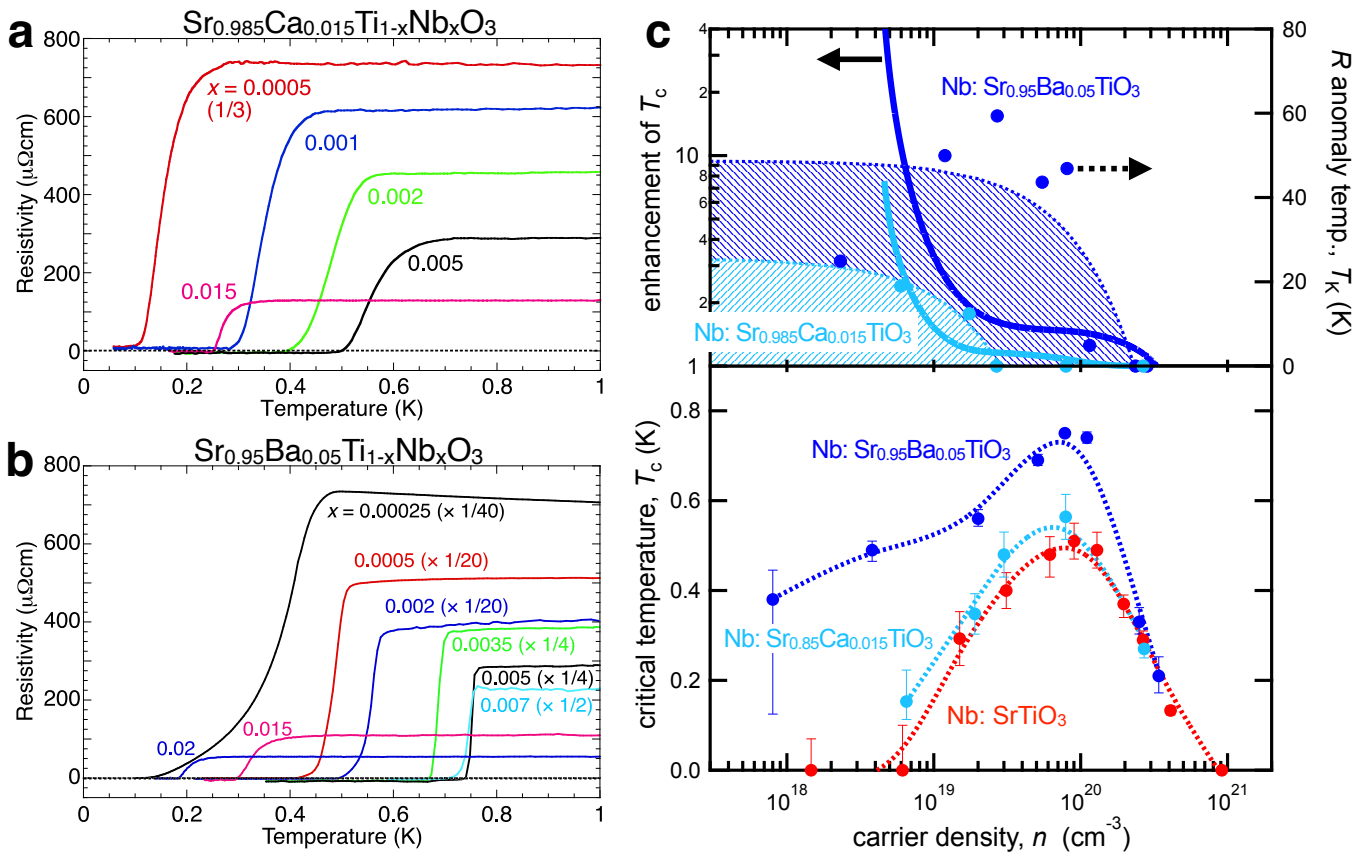


Fig. 4 | Superconductivity of the polar metals Nb:Sr_{0.985}Ca_{0.015}TiO₃ and Nb:Sr_{0.95}Ba_{0.05}TiO₃. **a**, Resistivity of the Sr_{0.985}Ca_{0.015}Ti_{1-x}Nb_xO₃ single crystals (same samples in Fig. 3a) below 1 K for 0.0005 $\leq x \leq$ 0.015. **b**, Resistivity of the Sr_{0.95}Ba_{0.05}Ti_{1-x}Nb_xO₃ single crystals (same samples in Fig. 3c) below 1 K for 0.00025 $\leq x \leq$ 0.02. **c**, The bottom panel depicts the superconducting domes of the polar metals, Nb:Sr_{0.985}Ca_{0.015}TiO₃ and Nb:Sr_{0.95}Ba_{0.05}TiO₃, plotted, for comparison, with that of the non-polar Nb:SrTiO₃ shown in Fig. 2b. Carrier density n of this plot was measured by the Hall effect at 5K. Dashed lines are obtained by smoothing spline interpolation. The top panel of Fig. 4c is a replot of T_K shown in Fig. 3b and Fig. 3d against the logarithmic values of n . The dashed lines correspond to the solid lines in Fig. 3b and Fig. 3d. The systems are polar in the hatched regions. The solid lines represent the ratios between T_c of the polar metals and that of the non-polar Nb:SrTiO₃.

Both of the polar metals, $\text{Nb:Sr}_{0.985}\text{Ca}_{0.015}\text{TiO}_3$ and $\text{Nb:Sr}_{0.95}\text{Ba}_{0.05}\text{TiO}_3$, show superconductivity at low temperatures. The resistive transition of the former is shown in Fig. 4a, and that of the latter is shown in Fig. 4b. The T_c values as a function of n at 5 K turn out the single superconducting dome as in Nb:SrTiO_3 (Fig. 4c, bottom). Moreover, the optimal T_c of $\text{Nb:Sr}_{0.95}\text{Ba}_{0.05}\text{TiO}_3$ reaches 0.75 K at $n \simeq 1 \times 10^{20} \text{ cm}^{-3}$. This is the highest T_c among the SrTiO_3 families ever reported. Furthermore, another interesting point is found in this viewgraph. Although the types of ferroelectricity are different in $\text{Sr}_{0.985}\text{Ca}_{0.015}\text{TiO}_3$ and $\text{Sr}_{0.95}\text{Ba}_{0.05}\text{TiO}_3$, and the ferroelectric QCP is one order different, only the low carrier-density region of the superconducting domes are shifted toward higher T_c in both cases. For clarity, we did a smoothing spline interpolation⁶⁵ (smoothing factor = 1) for the raw T_c data using the Igor Pro v8.04 software (WaveMetrics, Inc., USA). The dashed lines in the bottom panel of Fig. 4c represent the spline interpolations fitting the raw data very well. Using the interpolations, we deduced the T_c ratio between the polar and non-polar systems for each n , as shown by the solid lines in the top panel of Fig. 4c. We expected at first that the largest ratio would be seen around the ferroelectric QCP because we thought the quantum fluctuation could be the main driving force of superconductivity. However, the enhancement around the ferroelectric QCP is only about 1.2 – 1.5 for both the $\text{Nb:Sr}_{0.985}\text{Ca}_{0.015}\text{TiO}_3$ and $\text{Nb:Sr}_{0.95}\text{Ba}_{0.05}\text{TiO}_3$. Surprisingly, as the system goes deeper into the polar region where the ferroelectric fluctuations must be suppressed, the superconductivity is more enhanced.

Then, we suspected that defining the polar-metal region by T_K might not be appropriate, i.e., the real QCP may be elsewhere. Russel et al., however, reported that resistance anomaly temperature T_K of the strained $(\text{Sr,Sm})\text{TiO}_3$ film appears precisely at the same temperature at which the second harmonic generation (SHG) signal shows a sharp increase¹⁸. Since SHG indicates the inversion symmetry breaking of the system, it is reasonable to define the polar-metal region by T_K . Hence, our ferroelectric QCP where T_K becomes zero is well justified (Fig. 4c, top).

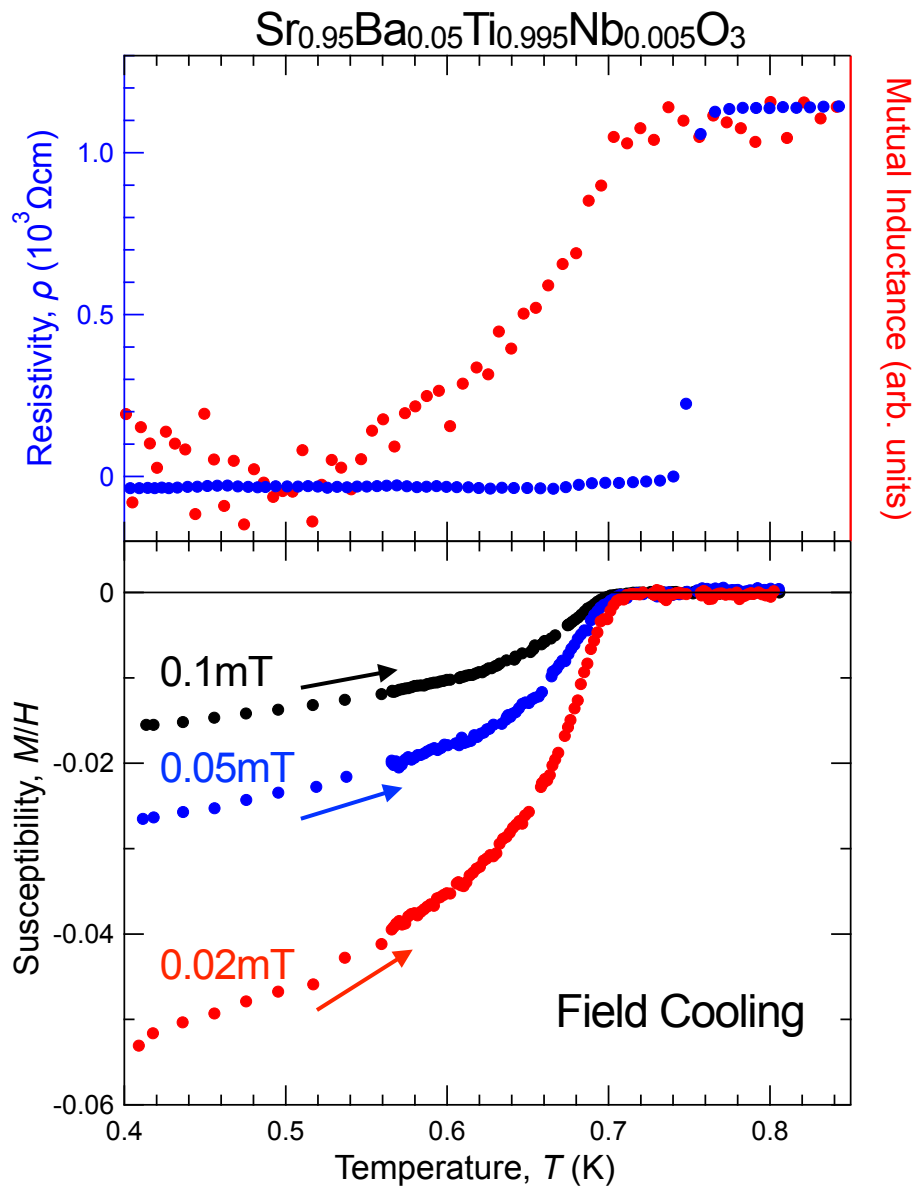


Fig. 5 | Comparison of the superconducting transition temperatures measured by resistivity, mutual inductance, and diamagnetism. The top panel shows the superconducting transition observed by the ac mutual inductance (red closed circles) for $\text{Sr}_{0.95}\text{Ba}_{0.05}\text{Ti}_{0.995}\text{Nb}_{0.005}\text{O}_3$ (same sample in Fig. 3c) below 0.9 K, compared with the resistive transition (blue closed circles) of the same sample. Although there must be an effect of the Joule heating due to the movement of the magnetic fluxes in the sample, the T_c value defined as the onset of the mutual inductance drop (0.70 K) is almost equal to the resistive one (0.75 K). The bottom panel shows the dc volume magnetic susceptibility (Meissner effect) measured while warming after the field cooling (FC) in 0.02, 0.05, and 0.1 mT for the same sample. The T_c value (0.70 K) defined as the onset of the diamagnetism nearly coincides with the zero resistivity temperature. (We have subtracted the background contribution. See the details in Methods).

So what contributes to the considerable enhancement of superconductivity away from QCP? A fascinating idea^{7,21,50} is to consider the intrinsic inhomogeneity in the region. Indeed, polar nanodomain formation is essential in most polar metals; small domains grow as the carrier density is decreased, and macroscopic ferroelectricity appears finally for the zero carrier-density limit¹⁹. It has been recently revealed that applying the uniaxial strain to the Nb:SrTiO₃ single crystal induces dislocations and local ferroelectricity with inhomogeneity resulting in the enhancement of the superconductivity²¹. The electroforming also creates metallic filaments, and the inhomogeneous structure raises the superconducting transition temperature⁵⁰.

However, the T_c value defined as the onset of the ac mutual inductance drop (0.70 K) for our Nb:Sr_{0.95}Ba_{0.05}TiO₃ single crystal ($n \sim 8.1 \times 10^{19} \text{ cm}^{-3}$) is almost equal to the resistive one (0.75 K), as shown in the top panel of Fig. 5, suggesting the T_c distribution is pretty homogeneous. In the bottom panel of Fig. 5, we plotted the dc volume susceptibility against temperature. After the successive field cooling (FC) down to about 0.4 K, the dc susceptibility was measured while warming. The onset of the diamagnetism is around 0.70 K, nearly coinciding with the zero resistivity temperature, indicating that the superconductivity of our Nb:Sr_{0.95}Ba_{0.05}TiO₃ can not be regarded as at least filamentary on the static timescale. Although the volume fraction of the Meissner effect (the reversible expulsion of magnetic flux in the FC measurement) looks small, it is almost comparable to the (Sr,La)TiO₃ ($n \sim 1.6 \times 10^{20} \text{ cm}^{-3}$) (ref.⁴⁰). This is simply because the applied magnetic field was not sufficiently small, but it is not an essential issue.

Bretz-Sullivan et al. have investigated⁴⁹ the single-crystalline SrTiO_{3- δ} in the dilute single band limit for $3.9 \times 10^{16} \text{ cm}^{-3} < n < 1.4 \times 10^{18} \text{ cm}^{-3}$. Although the system held three-dimensional homogeneous electron gas in the normal state, the superconducting state is inhomogeneous. Interestingly, for all the non-polar SrTiO_{3- δ} samples in the inhomogeneous superconducting region, the T_c values are not enhanced and are almost constant around 65 mK. The result means that the inhomogeneous superconductivity in the dilute carrier-density region is not the direct reason for the T_c enhancement; that is, the ferroelectric nature of the domains would be essential for the enhancement. For the two dimensional superconductivities in the LaAlO₃/SrTiO₃ interface, the Rashba spin-orbit coupling is the key to the Cooper pairing, i.e., the superconductivity requires inversion symmetry breaking⁶⁶. In the bulk SrTiO₃, the spin-orbit interaction is also essential^{6,17,23,44,67}, and the ferroelectricity arises from the centrosymmetry breaking¹⁷. Therefore, the bulk superconductivity may prefer more the space symmetry breaking against the Matthias Conjecture. In this sense, it is intriguing that the enigmatic 2 K superconductivity in the (111) surface of KTaO₃ is discussed as being related to the large spin-orbit interaction⁶⁸. Furthermore, according to this scenario, we may realise higher T_c by increasing the Ba contents to raise T_c^{FE} . Indeed, recent theoretical work on the carrier-doped BaTiO₃ has suggested that a significant

modulation of the electron-phonon coupling occurs across the polar-to-centrosymmetric phase transition, and superconductivity is predicted to appear at 2 K (ref.²⁰). Thus, we wonder the ferroelectric fluctuation around a single QCP may not be enough to enhance the superconductivity. However, the dynamical movement of the polar-domain boundaries can be regarded as a kind of spatiotemporal fluctuation of QCP. Hence, the lattice-polarity-superconductivity dynamics are to be further investigated to give a comprehensive view of the unique superconductivity of SrTiO₃.

We have confirmed that the Nb doping is an excellent method to dope carriers to SrTiO₃ with a smaller disorder, superior mobility, and higher T_c . Sr_{0.985}Ca_{0.015}TiO₃ and Sr_{0.95}Ba_{0.05}TiO₃ are different-type ferroelectrics, but the Nb-doping turns them polar metals with the resistance anomaly at T_K , which increases monotonically as the carrier-density decreases and coincides with the ferroelectric Curie temperature in the limit of zero carrier density. The quantum critical point, n^* , is derived from the T_K vs n relationship. Although the values of n^* for Nb:Sr_{0.985}Ca_{0.015}TiO₃ and Nb:Sr_{0.95}Ba_{0.05}TiO₃ are one order different, both of them show the typical single superconducting domes. Compared with the non-polar Nb:SrTiO₃, the values of T_c are enhanced. The enhancement ratio is less than 1.5 around QCP. However, it becomes much more prominent as going deeper into the ferroelectric region. These results challenge reconsidering the current models of the superconductivity in SrTiO₃.

References

1. Matthias, B. T. Superconductivity versus ferroelectricity. *Mater. Res. Bull.* **5**, 665–667 (1970).
2. Scheerer, G. *et al.* Ferroelectricity, Superconductivity, and SrTiO₃ — Passions of K.A. Müller. *Z. Phys. B: Condens. Matter* **5**, 60 (2020).
3. Zhou, W. X. & Ariando, A. Review on ferroelectric/polar metals. *Jpn. J. Appl. Phys.* **59**, SI0802 (2020).
4. Tomioka, Y., Shirakawa, N., Shibuya, K. & Inoue, I. H. Enhanced superconductivity close to a non-magnetic quantum critical point in electron-doped strontium titanate. *Nat. Commun.* **10**, 738 (2019).
5. Ahadi, K. *et al.* Enhancing superconductivity in SrTiO₃ films with strain. *Sci. Adv.* **5**, eaaw0120 (2019).
6. Schumann, T. *et al.* Possible signatures of mixed-parity superconductivity in doped polar SrTiO₃ films. *Phys. Rev. B* **101**, 100503 (2020).
7. Salmani-Rezaie, S., Jeong, H., Russell, R., Harter, J. W. & Stemmer, S. Role of locally polar regions in the superconductivity of SrTiO₃. *Phys. Rev. Mater.* **5**, 104801 (2021).
8. Wang, Y., Liu, X., Burton, J. D., Jaswal, S. S. & Tsymbal, E. Y. Ferroelectric instability under screened Coulomb interactions. *Phys. Rev. Lett.* **109**, 247601 (2012).

9. Stucky, A. *et al.* Isotope effect in superconducting n-doped SrTiO₃. *Sci. Rep.* **6**, 37582 (2016).
10. Rischau, C. W. *et al.* Isotope tuning of the superconducting dome of strontium titanate. *Phys. Rev. Research* **4**, 013019 (2022).
11. de Lima, B. S. *et al.* Interplay between antiferrodistortive, ferroelectric, and superconducting instabilities in Sr_{1-x}Ca_xTiO_{3-δ}. *Phys. Rev. B* **91**, 045108 (2015).
12. Rischau, C. W. *et al.* A ferroelectric quantum phase transition inside the superconducting dome of Sr_{1-x}Ca_xTiO_{3-δ}. *Nat. Phys.* **13**, 643–648 (2017).
13. Benedek, N. A. & Birol, T. ‘Ferroelectric’ metals reexamined: fundamental mechanisms and design considerations for new materials. *J. Mater. Chem.* **4**, 4000–4015 (2016).
14. Wang, J. *et al.* Charge transport in a polar metal. *npj Quantum Mater.* **4**, 61 (2019).
15. Arce-Gamboa, J. R. & Guzmán-Verri, G. G. Quantum ferroelectric instabilities in superconducting SrTiO₃. *Phys. Rev. Mater.* **2**, 104804 (2018).
16. Enderlein, C. *et al.* Superconductivity mediated by polar modes in ferroelectric metals. *Nat. Commun.* **11**, 4852 (2020).
17. Kanasugi, S., Kuzmanovski, D., Balatsky, A. V. & Yanase, Y. Ferroelectricity-induced multiorbital odd-frequency superconductivity in SrTiO₃. *Phys. Rev. B* **102**, 184506 (2020).
18. Russell, R. *et al.* Ferroelectric enhancement of superconductivity in compressively strained SrTiO₃ films. *Phys. Rev. Mater.* **3**, 091401 (2019).
19. Salmani-Rezaie, S., Ahadi, K. & Stemmer, S. Polar Nanodomains in a Ferroelectric Superconductor. *Nano Lett.* **20**, 6542–6547 (2020).
20. Ma, J., Yang, R. & Chen, H. A large modulation of electron-phonon coupling and an emergent superconducting dome in doped strong ferroelectrics. *Nat. Commun.* **12**, 2314 (2021).
21. Hameed, S. *et al.* Enhanced superconductivity and ferroelectric quantum criticality in plastically deformed strontium titanate. *Nat. Mater.* **21**, 54–61 (2022).
22. Collignon, C., Lin, X., Rischau, C. W., Fauqué, B. & Behnia, K. Metallicity and Superconductivity in Doped Strontium Titanate. *Annu. Rev. Condens. Matter Phys.* **10**, 25–44 (2019).
23. Gastiasoro, M. N., Ruhman, J. & Fernandes, R. M. Superconductivity in dilute SrTiO₃: A review. *Ann. Phys.* **417**, 168107 (2020).
24. Uwe, H. & Sakudo, T. Stress-induced ferroelectricity and soft phonon modes in SrTiO₃. *Phys. Rev.* **13**, 271–286 (1976).

25. Müller, K. A. & Burkard, H. SrTiO₃: An intrinsic quantum paraelectric below 4 K. *Phys. Rev. B* **19**, 3593–3602 (1979).
26. Watanabe, Y. Ferroelectricity of stress-free and strained pure SrTiO₃ revealed by ab initio calculations with hybrid and density functionals. *Phys. Rev. B* **99**, 064107 (2019).
27. Edge, J. M., Kedem, Y., Aschauer, U., Spaldin, N. A. & Balatsky, A. V. Quantum Critical Origin of the Superconducting Dome in SrTiO₃. *Phys. Rev. Lett.* **115**, 247002 (2015).
28. Rowley, S. E. *et al.* Ferroelectric quantum criticality. *Nat. Phys.* **10**, 367–372 (2014).
29. Coak, M. J. *et al.* Quantum critical phenomena in a compressible displacive ferroelectric. *Proc. Natl. Acad. Sci.* **117**, 12707–12712 (2020).
30. Bednorz, J. G. & Müller, K. A. Sr_{1-x}Ca_xTiO₃: An XY Quantum Ferroelectric with Transition to Randomness. *Phys. Rev. Lett.* **52**, 2289–2292 (1984).
31. Bianchi, U., Dec, J., Kleemann, W. & Bednorz, J. G. Cluster and domain-state dynamics of ferroelectric Sr_{1-x}Ca_xTiO₃ (x=0.007). *Phys. Rev. B* **51**, 8737–8746 (1995).
32. Lemanov, V. V., Smirnova, E. P., Syrnikov, P. P. & Tarakanov, E. A. Phase transitions and glasslike behavior in Sr_{1-x}Ba_xTiO₃. *Phys. Rev. B* **54**, 3151–3157 (1996).
33. Shirokov, V. B., Torgashev, V. I., Bakirov, A. A. & Lemanov, V. V. Concentration phase diagram of Ba_xSr_{1-x}TiO₃ solid solutions. *Phys. Rev. B* **73**, 104116 (2006).
34. Itoh, M. *et al.* Ferroelectricity Induced by Oxygen Isotope Exchange in Strontium Titanate Perovskite. *Phys. Rev. Lett.* **82**, 3540–3543 (1999).
35. Zubko, P., Catalan, G., Buckley, A., Welche, P. R. L. & Scott, J. F. Strain-gradient-induced polarization in SrTiO₃ single crystals. *Phys. Rev. Lett.* **99**, 167601 (2007).
36. Salje, E. K. H., Aktas, O., Carpenter, M. A., Laguta, V. V. & Scott, J. F. Domains within Domains and Walls within Walls: Evidence for Polar Domains in Cryogenic SrTiO₃. *Phys. Rev. Lett.* **111**, (2013).
37. Pertsev, N. A., Tagantsev, A. K. & Setter, N. Phase transitions and strain-induced ferroelectricity in SrTiO₃ epitaxial thin films. *Phys. Rev. B* **61**, R825–R829 (2000).
38. Haeni, J. H. *et al.* Room-temperature ferroelectricity in strained SrTiO₃. *Nature* **430**, 758–761 (2004).
39. Kang, K. T. *et al.* Ferroelectricity in SrTiO₃ epitaxial thin films via Sr-vacancy-induced tetragonality. *Appl. Surf. Sci.* **499**, 143930 (2020).
40. Suzuki, H. *et al.* Superconductivity in Single-Crystalline Sr_{1-x}La_xTiO₃. *J. Phys. Soc. Jpn.* **65**, 1529–1532 (1996).

41. Salmani-Rezaie, S. *et al.* Superconductivity in magnetically doped SrTiO₃. *Appl. Phys. Lett.* **118**, 202602 (2021).
42. Koonce, C. S., Cohen, M. L., Schooley, J. F., Hosler, W. R. & Pfeiffer, E. R. Superconducting Transition Temperatures of Semiconducting SrTiO₃. *Phys. Rev.* **163**, 380–390 (1967).
43. Binnig, G., Baratoff, A., Hoenig, H. E. & Bednorz, J. G. Two-Band Superconductivity in Nb-Doped SrTiO₃. *Phys. Rev. Lett.* **45**, 1352–1355 (1980).
44. Swartz, A. G. *et al.* Superconducting Tunneling Spectroscopy of Spin-Orbit Coupling and Orbital Depairing in Nb:SrTiO₃. *Phys. Rev. Lett.* **121**, 167003 (2018).
45. Schooley, J. F. *et al.* Dependence of the Superconducting Transition Temperature on Carrier Concentration in Semiconducting SrTiO₃. *Phys. Rev. Lett.* **14**, 305–307 (1965).
46. Schooley, J. F., Frederikse, H. P. R., Hosler, W. R. & Pfeiffer, E. R. Superconductive Properties of Ceramic Mixed Titanates. *Phys. Rev.* **159**, 301–305 (1967).
47. Lin, X. *et al.* Critical Doping for the Onset of a Two-Band Superconducting Ground State in SrTiO_{3-δ}. *Phys. Rev. Lett.* **112**, 207002 (2014).
48. Jourdan, M., Blümer, N. & Adrian, H. Superconductivity of SrTiO_{3-δ}. *Eur. Phys. J. B* **33**, 25–30 (2003).
49. Bretz-Sullivan, T. M. *et al.* Superconductivity in the dilute single band limit in reduced Strontium Titanate. *arXiv1904.03121* (2019).
50. Szot, K. *et al.* Filamentary superconductivity of resistively-switched strontium titanate. *arXiv2110.07230* (2021).
51. Gor'kov, L. P. Back to Mechanisms of Superconductivity in Low-Doped Strontium Titanate. *J. Supercond. Novel Magn.* **30**, 845–852 (2017).
52. van der Marel, D., Barantani, F. & Rischau, C. W. Possible mechanism for superconductivity in doped SrTiO₃. *Phys. Rev. Research* **1**, 013003 (2019).
53. van der Marel, D., van Mechelen, J. L. M. & Mazin, I. I. Common Fermi-liquid origin of T² resistivity and superconductivity in n-type SrTiO₃. *Phys. Rev. B* **84**, 205111 (2011).
54. Kumar, A., Yudson, V. I. & Maslov, D. L. Quasiparticle and Nonquasiparticle Transport in Doped Quantum Paraelectrics. *Phys. Rev. Lett.* **126**, 076601 (2021).
55. Takada, Y. Theory of Superconductivity in Polar Semiconductors and Its Application to N-Type Semiconducting SrTiO₃. *J. Phys. Soc. Jpn.* **49**, 1267–1275 (1980).
56. Ruhman, J. & Lee, P. A. Superconductivity at very low density: The case of strontium titanate. *Phys. Rev. B* **94**, 224515 (2016).

57. Tufte, O. N. & Chapman, P. W. Electron Mobility in Semiconducting Strontium Titanate. *Phys. Rev.* **155**, 796–802 (1967).
58. Frederikse, H. P. R. & Hosler, W. R. Hall Mobility in SrTiO₃. *Phys. Rev.* **161**, 822–827 (1967).
59. Spinelli, A., Torija, M. A., Liu, C., Jan, C. & Leighton, C. Electronic transport in doped SrTiO₃: Conduction mechanisms and potential applications. *Phys. Rev. B* **81**, 155110 (2010).
60. Behnia, K. On mobility of electrons in a shallow Fermi sea over a rough seafloor. *J. Phys. Condens. Matter* **27**, 375501 (2015).
61. Ricca, C., Timrov, I., Cococcioni, M., Marzari, N. & Aschauer, U. Self-consistent DFT study of oxygen vacancies in SrTiO₃. *Phys. Rev. Research* **2**, 023313 (2020).
62. Ma, M. & Lee, P. A. Localized superconductors. *Phys. Rev. B* **32**, 5658–5667 (1985).
63. Rodenbücher, C. *et al.* Mapping the conducting channels formed along extended defects in SrTiO₃ by means of scanning near-field optical microscopy. *Sci. Rep.* **10**, 17763 (2020).
64. Marrocchelli, D., Sun, L. & Yildiz, B. Dislocations in SrTiO₃: easy to reduce but not so fast for oxygen transport. *J. Am. Chem. Soc.* **137**, 4735–4748 (2015).
65. Reinsch, C. H. Smoothing by spline functions. *Numer. Math.* **10**, 177–183 (1967).
66. Caviglia, A. D. *et al.* Tunable Rashba spin-orbit interaction at oxide interfaces. *Phys. Rev. Lett.* **104**, 126803 (2010).
67. Noël, P. *et al.* Non-volatile electric control of spin-charge conversion in a SrTiO₃ Rashba system. *Nature* **580**, 483–486 (2020).
68. Liu, C. *et al.* Two-dimensional superconductivity and anisotropic transport at KTaO₃ (111) interfaces. *Science* **371**, 716–721 (2021).

Acknowledgements

This study was supported by the Japan Society for the Promotion of Science (JSPS) KAKENHI Grant Nos. 19H01844 (Category B) and 18H03686 (Category A), and was partially supported by the Japan Science and Technology Agency (JST) CREST Grant No. JPMJCR19K2. The authors would like to thank Hisashi Inoue, Keisuke Shibuya, and Reiji Kumai for helping us in the experiments, and Yaron Kedem, Jonathan Ruhman, Susanne Stemmer, Gian G. Guzmán-Verri and Siddharth (Montu) Saxena for stimulating discussion.

Author contributions

Y.T. and I.H.I. conceived the experiment. Y.T. performed the single crystal growth, x-ray diffraction, transport, and dielectric measurements. N.S. performed the diamagnetic measurement. The paper was written by Y.T. and I.H.I., with contributions from N.S.

Competing interests

The authors declare no competing interests.

Additional information

Correspondence and requests for materials should be addressed to I.H.I.

Methods

Single crystal growth. Mixed powders of SrCO₃, BaCO₃, TiO₂, and Nb₂O₅ in a ratio of 0.95 : 0.05 : 1-x : x/2 for Sr_{0.95}Ba_{0.05}Ti_{1-x}Nb_xO₃ (SrCO₃, CaCO₃, TiO₂, and Nb₂O₅ in a ratio of 0.985 : 0.015 : 1-x : x/2 for Sr_{0.985}Ca_{0.015}Ti_{1-x}Nb_xO₃) were calcined at 700 °C in air for a few hours. The calcined powders were sintered at 1000 °C in the air for five hours. Then, the powders were pulverised and formed into a rod, about 4 mm in diameter and about 50 mm in length. Each rod was fired at 1250 °C – 1350 °C for five hours in an argon gas flow. The crystal growth was conducted in a floating zone furnace with double hemi-ellipsoidal mirrors coated with gold. Two halogen lamps were used as the heat source. The crystals were grown in a stream of argon gas, and the growth rate was settled at 10 – 15 mm/h.

Structural analyses. Powder x-ray diffraction (XRD) patterns were collected on the Cu K α radiation diffractometer (SmartLab, Rigaku Co., Ltd) using the θ -2 θ step scanning method in the range of $15^\circ \leq 2\theta \leq 110^\circ$. The pattern indicated that the samples were of a single phase. For some crystals, Rietveld refinements for the lattice parameters and crystal symmetry were performed at various temperatures from 300 K to 10 K. Crystal alignments were done using back-reflection Laue diffraction. Results are summarised in Supplementary Information.

Transport properties. We cut the samples into rectangular shapes of $0.5 \times 0.3 \times 7 \text{ mm}^3$ with the longest edge parallel to the [100] direction of the cubic indices. Electrodes for the measurements were made by ultrasonic indium soldering, and the current was injected parallel to the [100] direction. The resistivity and the Hall voltage for $5 \text{ K} \leq T \leq 300 \text{ K}$ were measured in the Physical Property Measurement System (PPMS, Quantum Design Inc.). The resistivity below 1 K was measured using an ac resistance bridge (LR700, Linear Research Inc.) in a cryostat using a ³He/⁴He dilution refrigerator (μ dilution, Taiyo-Toyo Sanso Inc.).

Relative permittivity. Same as the transport measurements, the samples were cut along the [100] direction with the typical dimensions of $1.5 \times 0.4 \times 3 \text{ mm}^3$. The widest surface is the (110) plane, on which the electrodes were formed by painting and drying the silver paste. The relative permittivity for $5 \text{ K} \leq T \leq 300 \text{ K}$ were measured in PPMS.

Mutual inductance. The measurements were performed using the LR700 resistance bridge in a cryostat using a ³He/⁴He dilution refrigerator (μ dilution, Taiyo-Toyo Sanso Inc.). Induction (detection) coils with the diameter/length of 3 mm / 11 mm (2 mm / 6 mm) were set directly on the single crystals. We used a superconducting NbTi wire to avoid a possible temperature rise due to the Joule heating of the coils. The excitation current was 2 mA. The amplitude of the ac

magnetic field $\mu_0 H$ (μ_0 is the permeability of the vacuum) was estimated to be approximately 0.02 mT. The frequency was set at 15.9 Hz. Mutual inductance is proportional to the voltage of the detection coil, and the transition temperature is defined as the onset of the mutual inductance drop.

Diamagnetism. The dc magnetisation measurement for the Nb:Sr_{0.95}Ba_{0.05}TiO₃ single crystal ($n \sim 8.1 \times 10^{19} \text{ cm}^{-3}$) of $1.1 \times 1.1 \times 7.0 \text{ mm}^3$ was performed using a superconducting quantum interference device (SQUID) magnetometer (MPMS Quantum Design Inc.) equipped with a ³He refrigerator (iHelium 3, IQANTUM Inc.). The dc magnetic field was applied along the longest edge of the crystal parallel to the [100] direction of the pseudo-cubic lattice. The demagnetising factor along this direction is estimated to be less than 0.046 (ref.¹); thus, we can ignore the demagnetising effect. In the zero-field cooling (ZFC) protocol, the sample temperature was lowered to 0.4 K in zero field, and the dc magnetisation was measured in the presence of a static dc magnetic field $\mu_0 H$ of 0.02, 0.05, and 0.1 mT while warming the sample up to above T_c . In the field cooling (FC) protocol, the sample temperature was lowered to 0.4 K in the presence of $\mu_0 H$, and the dc magnetisation was measured in the static $\mu_0 H$ while warming. There is a tiny field-independent background in the magnetisation. Since the contributions from the sample to the SQUID signals are so small, the raw data are far from the ideal dipole response because of the background. We therefore subtracted a SQUID curve above T_c from the curves below T_c before performing the fitting.

Data availability

The data supporting this paper's plots and other findings of this study are available in figshare with the digital object identifier <https://doi.org/????> (the correct doi is given before the publication). Further data and resources are available from the corresponding authors upon reasonable request.

References

1. Osborn, J. A. Demagnetizing Factors of the General Ellipsoid. *Phys. Rev.* **67**, 351–357 (1945).

Supplementary Information

**Superconductivity enhanced in the polar metal region of
 $\text{Sr}_{0.95}\text{Ba}_{0.05}\text{TiO}_3$ and $\text{Sr}_{0.985}\text{Ca}_{0.015}\text{TiO}_3$
revealed by the systematic Nb doping.**

Yasuhide Tomioka, Naoki Shirakawa, and Isao H. Inoue

National Institute of Advanced Industrial Science and Technology (AIST),
Tsukuba 305-8565, Japan

Supplementary Note 1: Sample details for the $\text{SrTi}_{1-x}\text{Nb}_x\text{O}_3$ single crystals.

The Hall effect for our $\text{SrTi}_{1-x}\text{Nb}_x\text{O}_3$ single crystals was almost independent of temperature, and we plot the Hall resistivity ρ_H as a function of the magnetic field $\mu_0 H$ (μ_0 is the permeability of the vacuum) at 5 K in Fig. S1. The linear relationship yields the Hall coefficient $R_H = d\rho_H/d(\mu_0 H)$, and the carrier density n is evaluated using $R_H = (en)^{-1}$, where e is the elementary charge. The number of electrons per formula unit (f.u.) is deduced from n , almost equivalent to the nominal number of x , so we used this x value throughout the main text. The Hall mobility μ can be obtained by $\mu = (ne\rho)^{-1}$. Sample details and measured numbers obtained by our study for the $\text{SrTi}_{1-x}\text{Nb}_x\text{O}_3$ single crystals are summarised in Table S1.

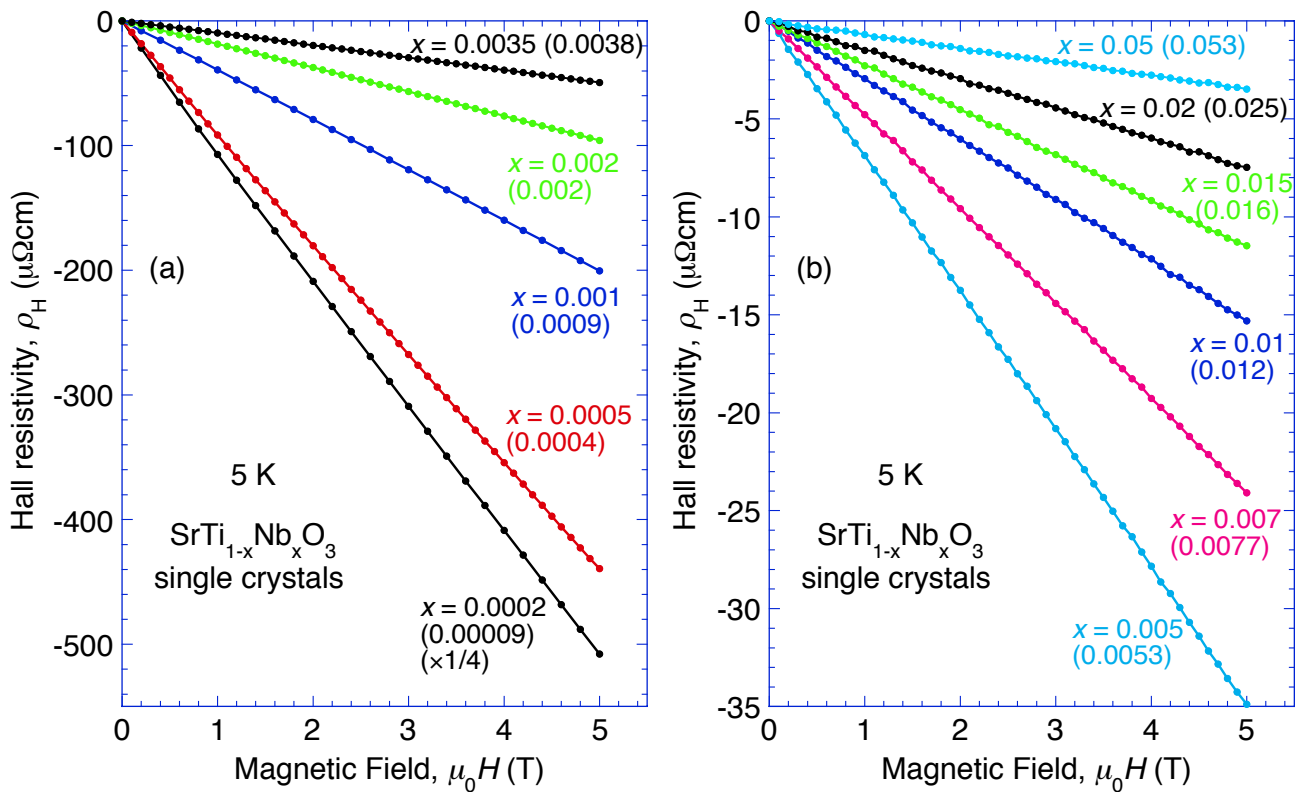


Fig. S1 | Hall effect at 5 K for $\text{SrTi}_{1-x}\text{Nb}_x\text{O}_3$ single crystals. Hall resistivity ρ_H versus magnetic field $\mu_0 H$ shows linear relationships. The number of electrons per formula unit was deduced from this plot and shown in the parenthesis.

Table S1 | Sample details for the SrTi_{1-x}Nb_xO₃ single crystals. Carrier density n (per formula unit and volume in cm³) determined from the Hall resistivity at 5K, the resistivity ρ at 300 K and 5 K, the Hall mobility μ at 5 K, and the critical temperature for superconductivity T_c obtained by our measurements.

x (nominal)	n (5 K) (per f.u.)	n (5 K) (cm ⁻³)	ρ (300 K) (Ω cm)	ρ (5 K) (Ω cm)	μ (5 K) (cm ² V ⁻¹ s ⁻¹)	T_c (K)
0.0002	0.000090	1.5×10^{18}	0.697	2.74×10^{-4}	15,000	(< 0.1)
0.0005	0.00040	7.0×10^{18}	0.176	9.49×10^{-5}	9,400	(< 0.1)
0.001	0.00090	1.6×10^{19}	0.0736	8.59×10^{-5}	4,700	0.29
0.002	0.0020	3.3×10^{19}	0.0351	8.38×10^{-5}	2,300	0.4
0.0035	0.0038	6.4×10^{19}	0.0188	8.17×10^{-5}	1,200	0.48
0.005	0.0053	9.0×10^{19}	0.0134	7.97×10^{-5}	870	0.51
0.007	0.0077	1.3×10^{20}	0.00872	7.69×10^{-5}	630	0.49
0.01	0.012	2.1×10^{20}	0.00554	6.72×10^{-5}	450	0.37
0.015	0.016	2.7×10^{20}	0.00377	5.68×10^{-5}	400	0.29
0.02	0.025	4.2×10^{20}	0.00247	4.96×10^{-5}	300	0.13
0.05	0.053	9.0×10^{20}	0.000963	4.86×10^{-5}	140	(< 0.1)

Supplementary Note 2: Temperature dependence of the carrier density for the $\text{Sr}_{0.95}\text{Ba}_{0.05}\text{Ti}_{1-x}\text{Nb}_x\text{O}_3$ and $\text{Sr}_{0.985}\text{Ca}_{0.015}\text{Ti}_{1-x}\text{Nb}_x\text{O}_3$ single crystals.

For the $\text{Sr}_{0.95}\text{Ba}_{0.05}\text{Ti}_{1-x}\text{Nb}_x\text{O}_3$ and $\text{Sr}_{0.985}\text{Ca}_{0.015}\text{Ti}_{1-x}\text{Nb}_x\text{O}_3$ single crystals (see the details below), the carrier density deduced from the Hall coefficient was plotted as a function of the temperature (Fig. S2). As for $\text{Sr}_{0.95}\text{Ba}_{0.05}\text{Ti}_{1-x}\text{Nb}_x\text{O}_3$, the carrier density decreases at low temperatures. The onsets of the carrier-density drop roughly correspond to the resistance anomaly temperatures T_K . On the contrary, in $\text{Sr}_{0.985}\text{Ca}_{0.015}\text{Ti}_{1-x}\text{Nb}_x\text{O}_3$, the drop of the carrier density is not apparent.

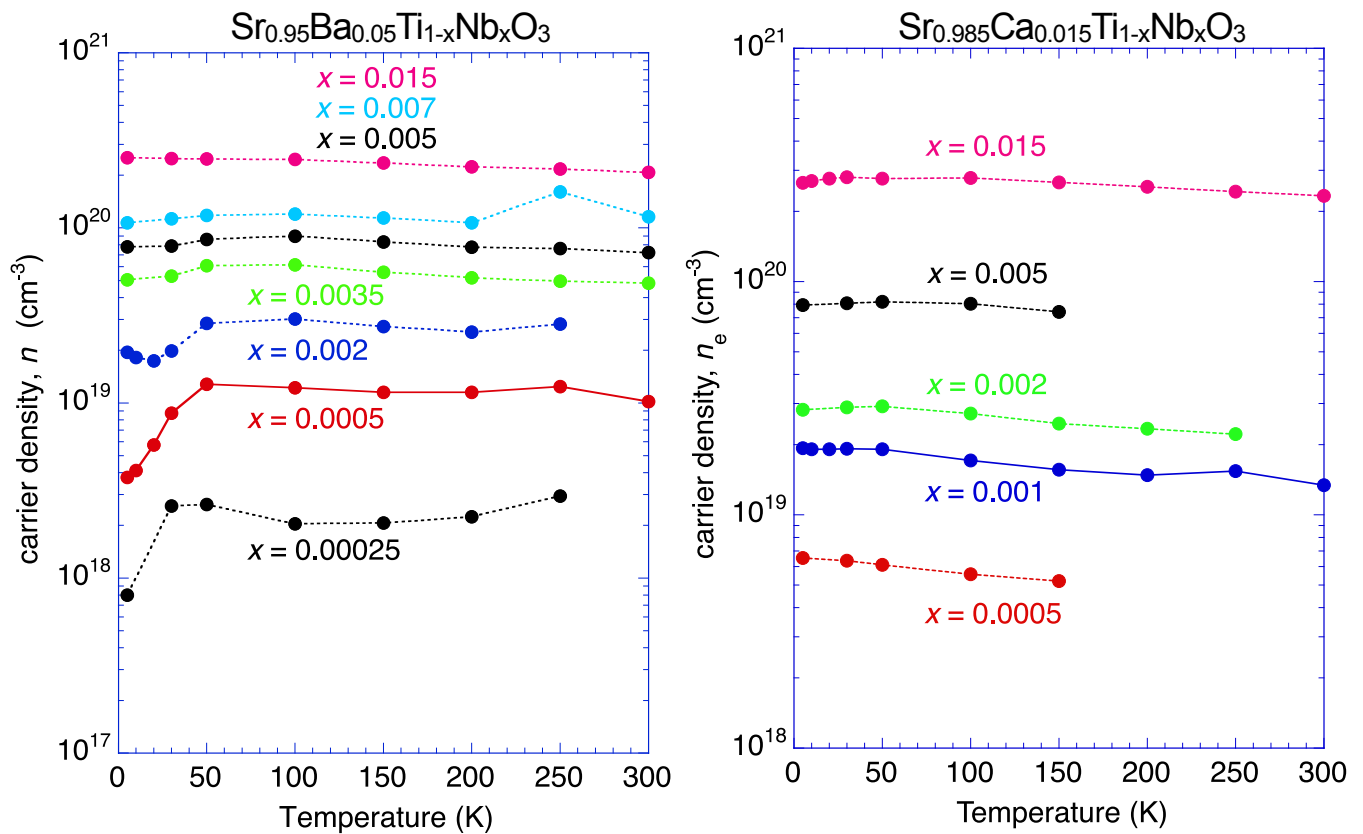


Fig. S2 | Temperature dependence of the carrier density for $\text{Sr}_{0.95}\text{Ba}_{0.05}\text{Ti}_{1-x}\text{Nb}_x\text{O}_3$ and $\text{Sr}_{0.985}\text{Ca}_{0.015}\text{Ti}_{1-x}\text{Nb}_x\text{O}_3$ single crystals. From the measured value of the Hall coefficient $R_H = d\rho_H/d(\mu_0 H)$, the carrier density n is evaluated as $R_H = (en)^{-1}$. In $\text{Sr}_{0.985}\text{Ca}_{0.015}\text{Ti}_{1-x}\text{Nb}_x\text{O}_3$, the temperature dependence is not apparent, whereas, in $\text{Sr}_{0.95}\text{Ba}_{0.05}\text{Ti}_{1-x}\text{Nb}_x\text{O}_3$, it decreases clearly at low temperatures at which the resistivity shows anomaly.

Supplementary Note 3: Sample details for the $\text{Sr}_{0.985}\text{Ca}_{0.015}\text{Ti}_{1-x}\text{Nb}_x\text{O}_3$ single crystals.

Same as $\text{SrTi}_{1-x}\text{Nb}_x\text{O}_3$, the Hall resistivity ρ_H at 5 K is linear to the magnetic field $\mu_0 H$, and the carrier density n is evaluated. The number of electrons per formula unit (f.u.) is almost equivalent to the nominal number of x , so we used this x value throughout the main text. The resistivity as a function of temperature shows an upturn for low carrier-density samples, and the temperature for the anomaly is denoted as T_K . Sample details and measured numbers obtained by our study for the $\text{Sr}_{0.985}\text{Ca}_{0.015}\text{Ti}_{1-x}\text{Nb}_x\text{O}_3$ single crystals are summarised in Table S2.

Table S2 | Sample details for the $\text{Sr}_{0.985}\text{Ca}_{0.015}\text{Ti}_{1-x}\text{Nb}_x\text{O}_3$ single crystals. Carrier density n (per formula unit and volume in cm^3) determined from the Hall resistivity at 5 K, the resistivity ρ at 300 K and 5 K, the resistance anomaly temperature T_K , and the critical temperature for superconductivity T_c obtained by our measurements.

x (nominal)	n (5 K) (per f.u.)	n (5 K) (cm^{-3})	ρ (300 K) (Ωcm)	ρ (5 K) (Ωcm)	T_K (K)	T_c (K)
0.0005	0.00040	6.5×10^{18}	0.227	0.00215	22.8	0.15
0.001	0.0010	1.9×10^{19}	0.151	0.000670	12.4	0.35
0.002	0.0017	2.8×10^{19}	0.0488	0.000475		0.48
0.005	0.0047	7.9×10^{19}	0.0168	0.000289		0.56
0.015	0.016	2.7×10^{20}	0.00457	0.000136		0.27

Supplementary Note 4: Sample details for the $\text{Sr}_{0.95}\text{Ba}_{0.05}\text{Ti}_{1-x}\text{Nb}_x\text{O}_3$ single crystals.

Same as $\text{SrTi}_{1-x}\text{Nb}_x\text{O}_3$ and $\text{Sr}_{0.985}\text{Ca}_{0.015}\text{Ti}_{1-x}\text{Nb}_x\text{O}_3$, the Hall resistivity ρ_H at 5 K is linear to the magnetic field $\mu_0 H$, and the carrier density n is evaluated. The number of electrons per formula unit (f.u.) is almost equivalent to the nominal number of x , so we used this x value throughout the main text. The resistivity as a function of temperature shows an upturn for low carrier-density samples, and the temperature for the anomaly is denoted as T_K . Sample details and measured numbers obtained by our study for the $\text{Sr}_{0.95}\text{Ba}_{0.05}\text{Ti}_{1-x}\text{Nb}_x\text{O}_3$ single crystals are summarised in Table S3.

Table S3 | Sample details for the $\text{Sr}_{0.95}\text{Ba}_{0.05}\text{Ti}_{1-x}\text{Nb}_x\text{O}_3$ single crystals. Carrier density n (per a formula unit and volume in cm^3) determined from the Hall resistivity at 5 K, the resistivity ρ at 300 K and 5 K, the resistance anomaly temperature T_K , and the critical temperature for superconductivity T_c obtained by our measurements.

x (nominal)	n (5 K) (per f.u.)	n (5 K) (cm^{-3})	ρ (300 K) (Ωcm)	ρ (5 K) (Ωcm)	T_K (K)	T_c (K)
0.00025	0.000050	8.0×10^{17}	0.717	0.0251	24.9	0.38
0.0005	0.00020	3.8×10^{18}	0.119	0.0113	49.9	0.49
0.002	0.0012	2.0×10^{19}	0.0506	0.00811	59.4	0.56
0.0035	0.0030	5.1×10^{19}	0.0215	0.00153	43.6	0.69
0.005	0.0046	7.8×10^{19}	0.0159	0.00120	46.9	0.75
0.007	0.0064	1.1×10^{20}	0.0135	0.000533	4.90	0.74
0.015	0.015	2.5×10^{20}	0.00467	0.000111		0.32
0.02	0.020	3.4×10^{20}	0.00304	5.50×10^{-5}		0.21

Supplementary Note 5: Ferroelectricity of $\text{Sr}_{0.95}\text{Ba}_{0.05}\text{TiO}_3$ and $\text{Sr}_{0.985}\text{Ca}_{0.015}\text{TiO}_3$ single crystals.

The non-doped $\text{Sr}_{0.95}\text{Ba}_{0.05}\text{TiO}_3$ and $\text{Sr}_{0.985}\text{Ca}_{0.015}\text{TiO}_3$ single crystals show the ferroelectric phase transition at 50 K and 24 K, respectively. The two ferroelectrics turn to polar metals with the resistance anomaly at low temperatures by doping a slight amount of Nb^{5+} for Ti^{4+} , i.e., by electron doping. Then, by further Nb doping, the resistance anomaly disappears at the critical carrier density n^* . We discuss in the main text that n^* corresponds to the quantum critical point (QCP). These values are summarised in Table S4.

Table S4 I Ferroelectric Curie temperature, the crystal symmetry of the ferroelectric phase (see below), the direction of polarisation, and carrier density at the quantum critical point (QCP) n^* above which the resistance anomaly disappears.

	Curie temp. (K)	crystal symmetry	polarization direction	QCP, n^* (cm^{-3})
$\text{Sr}_{0.95}\text{Ba}_{0.05}\text{TiO}_3$	50	$R\bar{3}m$	[111]	2.3×10^{20}
$\text{Sr}_{0.985}\text{Ca}_{0.015}\text{TiO}_3$	24	$P4mm$	[110]	2.8×10^{19}

Supplementary Note 6: Crystal structure of the $\text{Sr}_{0.95}\text{Ba}_{0.05}\text{Ti}_{0.998}\text{Nb}_{0.002}\text{O}_3$ single crystal.

Table S5 shows the crystallographic data for our metallic $\text{Sr}_{0.95}\text{Ba}_{0.05}\text{Ti}_{0.998}\text{Nb}_{0.002}\text{O}_3$ single crystals. The powder x-ray diffraction pattern was analysed assuming a trigonal $R\bar{3}m$ (hexagonal lattice) symmetry, and the results of the Rietveld refinement is summarised in Table S6. The atomic coordination (x, y, z) of the B-site of the ABO_3 formula unit is (0, 0, 0.4957), indicating that the displacement of the B-site occurs along the [001] direction of the hexagonal lattice that is equivalent to the [111] direction of a pseudo-cubic lattice. These results indicate that, for $\text{Sr}_{0.95}\text{Ba}_{0.05}\text{Ti}_{0.998}\text{Nb}_{0.002}\text{O}_3$, the crystal structure at low temperatures is consistent with trigonal $R\bar{3}m$, i.e., the centrosymmetry is broken as in the ferroelectric matrix $\text{Sr}_{0.95}\text{Ba}_{0.05}\text{TiO}_3$.

Table S5 | Crystallographic data of the $\text{Sr}_{0.95}\text{Ba}_{0.05}\text{Ti}_{0.998}\text{Nb}_{0.002}\text{O}_3$ single crystal. The lattice parameters can be expressed in the equivalent pseudo-cubic lattice as $a_R = 3.89826 \text{ \AA}$ and $\alpha = 90.00^\circ$.

formula weight (g)	186.061
density (g/cm^3)	5.2153
crystal system	Trigonal (hexagonal lattice)
space group	$R\bar{3}m$
lattice parameters (\AA)	$a = b = 5.51304, c = 6.75198, \alpha = \beta = 90^\circ, \gamma = 120^\circ$

Table S6 | Refined atomic parameters at 10 K of the $\text{Sr}_{0.95}\text{Ba}_{0.05}\text{Ti}_{0.998}\text{Nb}_{0.002}\text{O}_3$ single crystal. The Rietveld refinement was performed, converting the rhombohedral setting to a hexagonal one¹. The reliability factor² of the weighted profile $R_{wp} = 14.8$, and the patterns $R_p = 10.62$. The g and B_{eq} are the occupancy and isotropic displacement parameters, respectively.

atom	site	x	y	z	g	$B_{eq} (\text{\AA}^2)$
$\text{Sr}_{0.95}\text{Ba}_{0.05}$	$3a$	0	0	0	1	0.017
$\text{Ti}_{0.998}\text{Nb}_{0.002}$	$3a$	0	0	0.4957	1	0.033
O	$9b$	0.49965	0.50035	0.01457	1	0.006

Supplementary References

1. Izumi, F. & Momma, K. Three-dimensional visualization in powder diffraction. *Solid State Phenom.* **130**, 15–20 (2007).
2. Toby, B. H. R factors in Rietveld analysis: How good is good enough? *Powder Diffr.* **21**, 67–70 (2006).